Design and Optimization of High Misalignment Edge-Enhanced Stepped Coil Structure for Dynamic Wireless Power Transfer System

Chenxi ZHANG, Zhongqi LI, Jianbin WANG, and Changxuan HU

***Abstract*—In order to address the issue of mutual inductance variation in dynamic wireless power transfer systems for electric vehicles, which leads to significant fluctuations in system output, an edge-enhanced stepped coil structure is proposed to improve the system's anti-offset performance. Firstly, a model of the edge-enhanced stepped coil structure has been constructed, and the characteristics of mutual inductance variation for this structure have been analyzed. Secondly, a method for calculating mutual inductance in a stepped coil structure is proposed based on the Biot-Saval law. Then, based on the proposed method for calculating mutual inductance in stepped coils, the parameters of the edge-enhanced stepped coil structure are optimized according to the principle of minimizing fluctuations in mutual inductance. Additionally, a magnetic core structure that aligns with the coil's characteristics is designed to enhance both mutual inductance and the coil's resistance to offset performance. Finally, a 500 W experimental prototype has been constructed. The experimental results show that the mutual inductance fluctuation rate of the edge-enhanced stepped coil does not exceed 5% when the *Y*-axis direction is offset by 50% (362 mm) of the outer diameter of the transmitter coil. The transmission efficiency of the system is as high as 93.92%, and the fluctuation rate of the output current is less than 5%.**

***Index Terms*—High misalignment tolerance; mutual inductance calculation; stepped coil structure; wireless power transfer.**

I. Introduction

WIRELESS power transfer (WPT) technology enables the non-contact transfer of energy using electromagnetic fields and alternative media, providing an innovative solution to the safety and convenience issues associated with traditional contact charging methods [1]–[3]. WPT technology has attracted considerable attention from researchers both domestically and internationally due to its remarkable flexibility, high safety and reliability, and its ability to function effectively in harsh environmental conditions. Currently, WPT technology has been successfully applied across various domains, including underwater power supply systems for equipment [4]–[6], consumer electronics [7]–[9], and intelligent rail transit systems [10]–[11].

In dynamic WPT, positional shifts of the coupling coil result in variations in mutual inductance between the coils. These fluctuations negatively impact the stable operation of the WPT system, presenting challenges to its reliability and safety [12]–[14]. In response to the aforementioned issues, researchers have conducted extensive studies on the anti-offset performance of coils, with the goal of improving the stability and reliability of the system when the coil position is misaligned. Consequently, investigating coil structures that exhibit quasi-constant mutual inductance is of great significance.

The classification of coils depends on the number of coils present. Coils can be categorized as either single-coil or multi-coil structures. The magnetic field produced by the single-coil structure is unidirectional. Consequently, when the coil is misaligned, the positive area of the coil decreases, leading to a reduction in positive magnetic flux. When the misalignment reaches half the diameter of the transmitting coil, there is not only a decrease in positive magnetic flux but also the emergence of negative magnetic flux, which compromises the anti-offset performance. The offset performance of the single-coil structure is enhanced through the optimization of coil size [15]–[17], turn spacing and core structure [18]–[20].

The multi-coil structure leverages the spatial superposition of multiple coils, employing the principle of magnetic field superposition to enhance effective coupling and improve the coil's resistance to offset performance. A team from the University of Auckland, New Zealand, proposed a double-D (DD) coil, which consists of two unipolar coils connected in series and placed side by side. They also incorporated an orthogonal Q-type coil into the DD coil to create a double-D quadrature (DDQ) coil structure. This design effectively compensates for the induction blindness inherent in the DD coil [21]. In addition, to reduce consumable materials, the team proposed

Manuscript received March 23, 2025; revised July 01, 2025; accepted July 11, 2025. Date of publication September 30, 2025; date of current version August 22, 2025. This work was supported in part by National Key R&D Program Project under the grant 2022YFB3403200, Key Projects of Hunan Provincial Department of Education under the grant 23A0432, Excellent Youth Project of Scientific Research of Hunan Provincial Department of Education under the grant 22B0577, National Natural Science Foundation of China (NSFC) Youth Science Fund Project under the grant 62303178, and A Project Supported by Scientific Research Fund of Hunan Provincial Education Department under the grant 23C0182. (*Corresponding authors: Zhongqi Li.*)

All authors are with the School of Transportation and Electrical Engineering, Hunan University of Technology, Zhuzhou 412007, China (e-mail:17873436232@163.com; lizhongqi@hnu.edu.cn; 1366597990@qq.com; 905436194@qq.com).

Digital Object Identifier 10.24295/CPSSTPEA.2025.00024

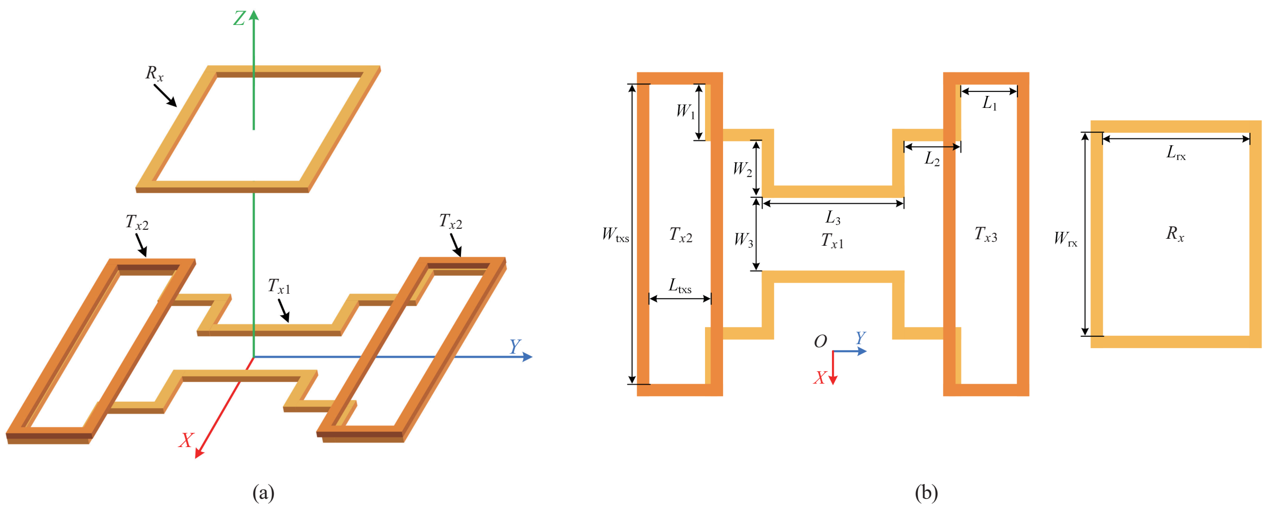

Fig. 1. EESC structure diagram. (a) 3D structural model. (b) Top view of structure.

the bipolar (BP) coil structure in [22] and the tripolar (TP) coil structure in [23], utilizing coil stacking. This approach can enhance the coil offset performance to some extent.

Researchers have investigated more advanced coil structures by employing modular combination strategies. One notable design is the double-layer quadrature double-D(DQDD) structure, which consists of two pairs of DD coils arranged orthogonally in a double-layer configuration. This arrangement facilitates decoupling between the coils and creates a periodic variation in the excited magnetic field. However, the DQDD structure exhibits a coupling coefficient fluctuation of 55% under a horizontal offset of 150 mm, indicating that its anti-offset performance is insufficient to withstand significant positional shifts [24]. In addition to the above magnetic field superposition approach, researchers have exploited the feature that the reverse series coil has the opposite tendency to the forward coil with coil offset to achieve a largely constant mutual inductance during coil offset. A multi-receiver reverse series coil structure has been proposed, and by optimizing the forward and reverse series coils, the mutual inductance fluctuation is only 3.81% when the coil is offset by 34% (225 mm) of the maximum coil outer length [25].

In summary, most current coil structures accommodate a limited offset range during static charging. However, there are issues related to the small maximum allowable offset distance of the coupling coil and the significant fluctuations in mutual inductance that occur during coil offset in dynamic wireless power transfer. The contributions of this paper are as follows:

1) An edge-enhanced stepped coil structure is proposed, an edge-enhanced stepped coil structure model is dissected, and the mutual inductance characteristics of the edge-enhanced stepped coil structure are analyzed.

2) Stepped coils are modelled and a method for calculating the mutual inductance of stepped transmitting coils and rectangular receiving coils based on the Biot-Saval law is proposed.

3) An optimisation strategy based on the principle of minimising mutual inductance fluctuations is proposed, aiming to optimise the coil sizing parameters and core sizing parameters, with the objective of achieving the maximum coil offset distance of 50% of the length of the outer diameter of the transmitting coil and a mutual inductance fluctuation rate of less than 5%.

4) The 500 W experimental prototype is built, and the experiment proves that the proposed coil structure has good anti-offset performance, and the output of the system is smooth.

In this paper, the structural model of the edge-enhanced stepped coil is given and analyzed in Section II. The formula for calculating the mutual inductance of the stepped coil in Section III. The experimental verification in Section IV. Finally, the conclusions are shown in Section V.

II. Edge-Enhanced Stepped Coil Structure

A. Structure Model

In this paper, an edge-enhanced stepped coil structure is proposed in order to achieve a larger limit offset range of the coupling coil in dynamic wireless power transfer system and to keep the mutual inductance quasi-constant within the limit offset range. The EESC structure employs a stepped coil as the main coil and applies the principle of magnetic field superposition to introduce isotropic series compensation coils at the edges of the stepped coil, with the objective of enhancing the mutual inductance at the edges of the main coil. A three-dimensional representation of the EESC structure is presented in Fig. 1(a). The transmitter coil (T_x) consists of a step coil (T_{x1}) and two compensation coils (T_{x2} and T_{x3}),compensation coils are arranged in a stacked configuration along step coil in the Y-axis direction. The receiving coil (R_x) is a rectangular coil.

The plan view of the EESC coil structure is illustrated in Fig. 1(b). The coil parameter variables are defined as follows: L_1, L_2, and L_3 will be used to denote the length of the stepped coil T_{x1}. W_1, W_2, and W_3 will be used to denote the width of the same coil. L_{txs} and W_{txs} will be used to denote the length and width of compensation coils T_{x2} and T_{x3}, respectively. L_{rx} and

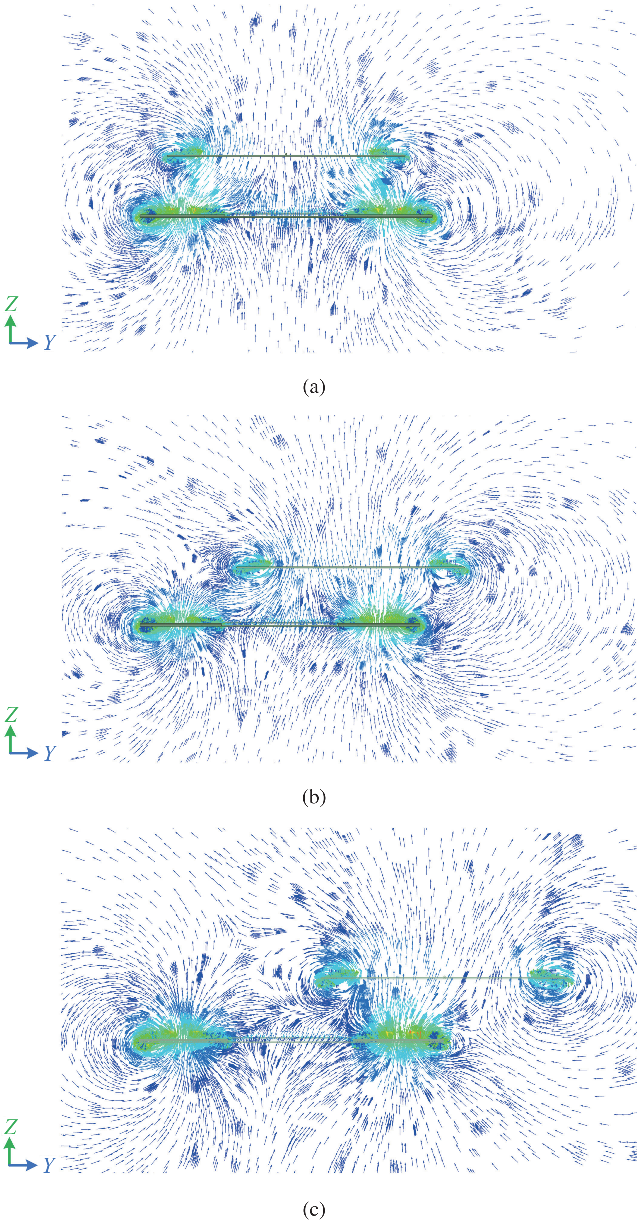

Fig. 2. EESC magnetic field diagrams at offset along the Y-axis direction. (a) $\Delta Y = 0$. (b) $\Delta Y = 0.25L_{\text{tx-o}}$. (c) $\Delta Y = 0.5L_{\text{tx-o}}$.

W_{rx} will be used to denote the length and width of the receiver coil R_x, respectively. In order to guarantee optimal anti-offset functionality when the coils are offset, compensation coils are of identical dimensions and arranged in a symmetrical fashion to align the outer edges of the main coils.

The stepped coil is designed with three distinct levels, which progressively extend along the Y-axis and result in an increased coil width along the X-axis. This design effectively increases the positive overlap area between the transmitting and receiving coils when an offset occurs. Consequently, a larger longitudinal flux passes through the coils, enabling the mutual inductance to be preserved to a significant extent. Compared to conventional rectangular coils, the stepped coil demonstrates enhanced anti-offset performance, making it a more robust option for dynamic wireless power transfer systems.

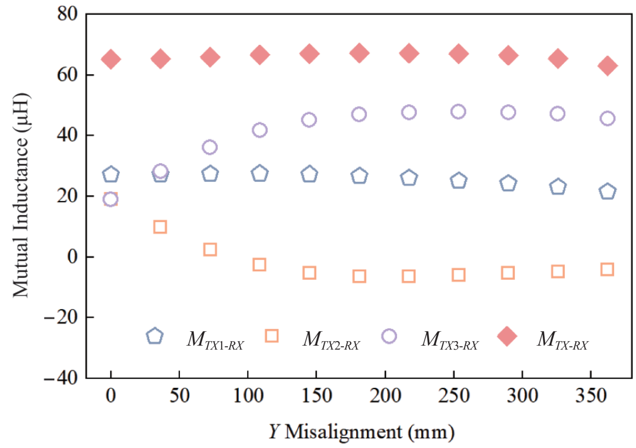

Fig. 3. Variation curves of mutual inductance at offset along the Y-axis direction.

B. Mutual Inductance Characterisation of Coil Structures

To evaluate the anti-offset performance of the EESC structure, a simulation model was developed using ANSYS Maxwell software. The magnetic field distribution is simulated in the Y-axis, as illustrated in Fig. 2. ΔY denotes the offset distance along the Y-axis direction, $L_{\text{tx-o}}$ denotes the outer diameter length of the transmitter coil.

When the transmitting and receiving coils are perfectly aligned ($\Delta Y = 0$) in Fig. 2(a), the transmitting coil generates a longitudinal magnetic flux that passes vertically through the receiving coil, facilitating effective coupling between the coils. As the receiving coil offsets along the positive Y-axis ($\Delta Y = 0.25L_{\text{tx-o}}$) in Fig. 2(b), it gradually shifts from the center toward the edge. During this shift, the area directly opposite the receiving coil on compensating coil T_{x2} decreases, while the area directly opposite compensating coil T_{x3} increases. Through the principle of magnetic field superposition, this redistribution enhances the total magnetic flux across the three coils, thereby increasing the mutual inductance. When the offset continues in a positive direction along the Y-axis ($\Delta Y = 0.5L_{\text{tx-o}}$) in Fig. 2(c), the longitudinal flux through the receiving coil R_x gradually diminishes. Consequently, the total magnetic flux and the mutual inductance between the coils also decrease.

Fig. 3 shows the mutual inductance variation curves for horizontal offset along the positive direction of Y-axis between the receiving coil R_x and the main coil T_{x1}, the compensation coil T_{x2} and the compensation coil T_{x3}, respectively. The mutual inductance expression between the EESC coupling mechanism is shown in (1).

$$M_{TX\text{-}RX} = M_{TX1\text{-}RX} + M_{TX2\text{-}RX} + M_{TX3\text{-}RX} \tag{1}$$

where M_{TX-RX} is the mutual inductance between T_x and R_x, $M_{TX1\text{-}RX}$ is the mutual inductance between T_{x1} and R_x, $M_{TX2\text{-}RX}$ is the mutual inductance between T_{x2} and R_x, and $M_{TX3\text{-}RX}$ is the mutual inductance between T_{x3} and R_x.

As the offset distance increases, $M_{TX1\text{-}RX}$ and $M_{TX2\text{-}RX}$ gradually decrease, $M_{TX3\text{-}RX}$ exhibits a significant increasing trend. The $M_{TX\text{-}RX}$ remains basically stable in the limit offset range. During

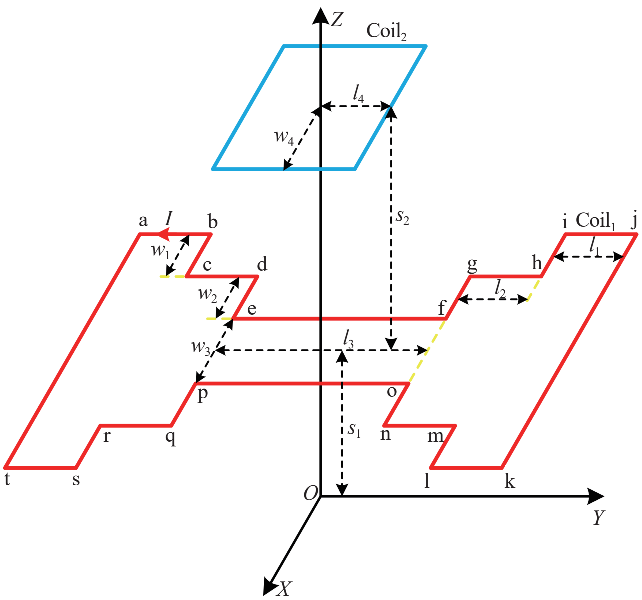

Fig. 4. EESC structure diagrams.

the coil offset process, the magnetic field superposition principle is used to superimpose the magnetic flux through the receiving coil to form a region where the mutual inductance of the coils increases and then decreases. This ensures that the mutual inductance between the coils is quasi-constant.

III. Calculation of Mutual Inductance of Stepped Coils

In order to study the working mechanism of the EESC structure under different offsets and its offset characteristics, it is necessary to create a model of the coil structure. However, there is currently no established methodology for calculating the mutual inductance of stepped coils. Such a model would provide a theoretical foundation for understanding the performance of the EESC structure and optimizing its design for improved anti-offset capabilities.

As shown in Fig. 4, the transmitting coil is a stepped coil, the receiving coil is a rectangular coil. l_1, l_2, and l_3 are the lengths of the different echelons of the stepped coil. w_1, w_2, and w_3 are the widths of the different echelons of the stepped coil. l_4 and w_4 are the lengths and widths of the rectangular receiving coil. s_1 is the vertical distance between the stepped coil O_1 and O. s_2 is the vertical distance between the rectangular coil O_2 and O_1.

Setting any point $P(x, y, z)$ in the plane of the receiving coil, the magnetic flux density generated by the transmitting coil at P inside the receiving coil can be expressed according to the Biot-Saval law:

$$\vec{B}=\frac{\mu_0 I}{4\pi}\oint_{C'}\left(\frac{\mathrm{d}\vec{l}'\times\vec{R}}{R^3}\right) \tag{2}$$

where μ_0 is the magnetic permeability in vacuum, I is the current on the transmitting coil, C' is the curve enclosed by the transmitting coil, $I\mathrm{d}\vec{l}'$ denotes the current element, $\vec{R}$ is the distance vector from any point P to the current element. $I\mathrm{d}\vec{l}'\times\vec{R}$ can be calculated in (3) to (5).

$$\begin{cases}
\mathrm{d}\vec{l}'_{ab}=-\mathrm{d}y'\hat{y},\ \mathrm{d}\vec{l}'_{bc}=-\mathrm{d}x'\hat{x},\ \mathrm{d}\vec{l}'_{cd}=-\mathrm{d}y'\hat{y},\ \mathrm{d}\vec{l}'_{de}=-\mathrm{d}x'\hat{x}\\
\mathrm{d}\vec{l}'_{ef}=-\mathrm{d}y'\hat{y},\ \mathrm{d}\vec{l}'_{fg}=\mathrm{d}x'\hat{x},\ \mathrm{d}\vec{l}'_{gh}=-\mathrm{d}y'\hat{y},\ \mathrm{d}\vec{l}'_{hi}=\mathrm{d}x'\hat{x}\\
\mathrm{d}\vec{l}'_{ij}=-\mathrm{d}y'\hat{y},\ \mathrm{d}\vec{l}'_{jk}=-\mathrm{d}x'\hat{x},\ \mathrm{d}\vec{l}'_{kl}=\mathrm{d}y'\hat{y},\ \mathrm{d}\vec{l}'_{lm}=\mathrm{d}x'\hat{x}\\
\mathrm{d}\vec{l}'_{mn}=\mathrm{d}y'\hat{y},\ \mathrm{d}\vec{l}'_{no}=\mathrm{d}x'\hat{x},\ \mathrm{d}\vec{l}'_{op}=\mathrm{d}y'\hat{y},\ \mathrm{d}\vec{l}'_{pq}=-\mathrm{d}x'\hat{x}\\
\mathrm{d}\vec{l}'_{pr}=\mathrm{d}y'\hat{y},\ \mathrm{d}\vec{l}'_{rs}=-\mathrm{d}x'\hat{x},\ \mathrm{d}\vec{l}'_{st}=\mathrm{d}y'\hat{y},\ \mathrm{d}\vec{l}'_{ta}=-\mathrm{d}x'\hat{x}
\end{cases} \tag{3}$$

$$\begin{cases}
\vec{R}_{ab}=(x+(w_1+w_2+w_3/2))\hat{x}+(y-y')\hat{y}+z\hat{z}\\
\vec{R}_{bc}=(x-x')\hat{x}+(y+(l_2+l_3/2))\hat{y}+z\hat{z}\\
\vec{R}_{cd}=(x+(w_2+w_3/2))\hat{x}+(y-y')\hat{y}+z\hat{z}\\
\vec{R}_{de}=(x-x')\hat{x}+(y+(l_3/2))\hat{y}+z\hat{z}\\
\vec{R}_{ef}=(x+(w_3/2))\hat{x}+(y-y')\hat{y}+z\hat{z}\\
\vec{R}_{fg}=(x-x')\hat{x}+(y-(l_3/2))\hat{y}+z\hat{z}\\
\vec{R}_{gh}=(x+(w_2+w_3/2))\hat{x}+(y-y')\hat{y}+z\hat{z}\\
\vec{R}_{hi}=(x-x')\hat{x}+(y-(l_2+l_3/2))\hat{y}+z\hat{z}\\
\vec{R}_{ij}=(x+(w_1+w_2+w_3/2))\hat{x}+(y-y')\hat{y}+z\hat{z}\\
\vec{R}_{jk}=(x-x')\hat{x}+(y-(l_1+l_2+l_3/2))\hat{y}+z\hat{z}\\
\vec{R}_{kl}=(x-(w_1+w_2+w_3/2))\hat{x}+(y-y')\hat{y}+z\hat{z}\\
\vec{R}_{lm}=(x-x')\hat{x}+(y-(l_2+l_3/2))\hat{y}+z\hat{z}\\
\vec{R}_{mn}=(x-(w_2+w_3/2))\hat{x}+(y-y')\hat{y}+z\hat{z}\\
\vec{R}_{no}=(x-x')\hat{x}+(y-(l_3/2))\hat{y}+z\hat{z}\\
\vec{R}_{op}=(x-(w_3/2))\hat{x}+(y-y')\hat{y}+z\hat{z}\\
\vec{R}_{pq}=(x-x')\hat{x}+(y+(l_3/2))\hat{y}+z\hat{z}\\
\vec{R}_{qr}=(x-(w_2+w_3/2))\hat{x}+(y-y')\hat{y}+z\hat{z}\\
\vec{R}_{rs}=(x-x')\hat{x}+(y+(l_2+l_3/2))\hat{y}+z\hat{z}\\
\vec{R}_{st}=(x-(w_1+w_2+w_3/2))\hat{x}+(y-y')\hat{y}+z\hat{z}\\
\vec{R}_{ta}=(x-x')\hat{x}+(y+(l_1+l_2+l_3/2))\hat{y}+z\hat{z}
\end{cases} \tag{4}$$

$$\begin{cases}
\mathrm{d}l'_{ab}\times\vec{R}_{ab}=-z\mathrm{d}y'\hat{x}+\mathrm{d}y'(x+(w_1+w_2+w_3/2))\hat{z}\\
\mathrm{d}l'_{bc}\times\vec{R}_{bc}=z\mathrm{d}x'\hat{y}-\mathrm{d}x'(y+(l_2+l_3/2))\hat{z}\\
\mathrm{d}l'_{cd}\times\vec{R}_{cd}=-z\mathrm{d}y'\hat{x}+\mathrm{d}y'(x+(w_2+w_3/2))\hat{z}
\end{cases} \tag{5}$$

$$\begin{cases} dl'_{de}\times\vec{R}_{de}=zdx'\hat{y}-dx'(y+(l_3/2))\hat{z} \\ dl'_{ef}\times\vec{R}_{ef}=-zdy'\hat{x}+dy'(x+(w_3/2))\hat{z} \\ dl'_{fg}\times\vec{R}_{fg}=-zdx'\hat{y}+dx'(y-(l_3/2))\hat{z} \\ dl'_{gh}\times\vec{R}_{gh}=-zdy'\hat{x}+dy'(x+(w_2+w_3/2))\hat{z} \\ dl'_{hi}\times\vec{R}_{hi}=-zdx'\hat{y}+dx'(y-(l_2+l_3/2))\hat{z} \\ dl'_{ij}\times\vec{R}_{ij}=-zdy'\hat{x}+dy'(x+(w_1+w_2+w_3/2))\hat{z} \\ dl'_{jk}\times\vec{R}_{jk}=zdx'\hat{y}-dx'(y-(l_1+l_2+l_3/2))\hat{z} \\ dl'_{kl}\times\vec{R}_{kl}=zdy'\hat{x}-dy'(x-(w_1+w_2+w_3/2))\hat{z} \\ dl'_{lm}\times\vec{R}_{lm}=-zdx'\hat{y}+dx'(y-(l_2+l_3/2))\hat{z} \\ dl'_{mn}\times\vec{R}_{mn}=zdy'\hat{x}-dy'(x-(w_2+w_3/2))\hat{z} \\ dl'_{no}\times\vec{R}_{no}=-zdx'\hat{y}+dx'(y-(l_3/2))\hat{z} \\ dl'_{op}\times\vec{R}_{op}=zdy'\hat{x}-dy'(x-(w_3/2))\hat{z} \\ dl'_{pq}\times\vec{R}_{pq}=zdx'\hat{y}-dx'(y+(l_3/2))\hat{z} \\ dl'_{qr}\times\vec{R}_{qr}=zdy'\hat{x}-dy'(x-(w_2+w_3/2))\hat{z} \\ dl'_{rs}\times\vec{R}_{rs}=zdx'\hat{y}-dx'(y+(l_2+l_3/2))\hat{z} \\ dl'_{st}\times\vec{R}_{st}=zdy'\hat{x}-dy'(x-(w_1+w_2+w_3/2))\hat{z} \\ dl'_{ta}\times\vec{R}_{ta}=-zdx'\hat{y}-dx'(y+(l_1+l_2+l_3/2))\hat{z} \end{cases} \tag{5}$$

The magnetic flux density generated by each line segment of the stepped coil at any point P can be obtained by substituting (4) into (1). The magnetic flux density at any point P in the Z-axis direction can be expanded according to (1) as follows:

$$B_{ab}=\frac{\mu_0 N_1 I}{4\pi}\left(\frac{(x+(w_1+w_2+w_3/2))}{(x+(w_1+w_2+w_3/2))^2+z^2}\right)\times \left(\frac{y+(l_1+l_2+l_3/2)}{R_a}-\frac{y+(l_2+l_3/2)}{R_b}\right) \tag{6}$$

$$B_{bc}=\frac{\mu_0 N_1 I}{4\pi}\left(\frac{-(y+(l_2+l_3/2))}{(y+(l_2+l_3/2))^2+z^2}\right)\times \left(\frac{x+(w_1+w_2+w_3/2)}{R_b}-\frac{x+(w_2+w_3/2)}{R_c}\right) \tag{7}$$

$$B_{cd}=\frac{\mu_0 N_1 I}{4\pi}\left(\frac{(x+(w_2+w_3/2))}{(x+(w_2+w_3/2))^2+z^2}\right)\times \left(\frac{y+(l_2+l_3/2)}{R_c}-\frac{y+(l_3/2)}{R_d}\right) \tag{8}$$

$$B_{de}=\frac{\mu_0 N_1 I}{4\pi}\left(\frac{-(y+(l_3/2))}{(y+(l_3/2))^2+z^2}\right)\times \left(\frac{x+(w_2+w_3/2)}{R_d}-\frac{x+(w_3/2)}{R_e}\right) \tag{9}$$

$$B_{ef}=\frac{\mu_0 N_1 I}{4\pi}\left(\frac{(x+(w_3/2))}{(x+(w_3/2))^2+z^2}\right)\times \left(\frac{y+(l_3/2)}{R_e}-\frac{y-(l_3/2)}{R_f}\right) \tag{10}$$

$$B_{fg}=\frac{\mu_0 N_1 I}{4\pi}\left(\frac{-(y-(l_3/2))}{(y-(l_3/2))^2+z^2}\right)\times \left(\frac{x+(w_3/2)}{R_f}-\frac{x+(w_2+w_3/2)}{R_g}\right) \tag{11}$$

$$B_{gh}=\frac{\mu_0 N_1 I}{4\pi}\left(\frac{(x+(w_2+w_3/2))}{(x+(w_2+w_3/2))^2+z^2}\right)\times \left(\frac{y-(l_3/2)}{R_g}-\frac{y-(l_2+l_3/2)}{R_h}\right) \tag{12}$$

$$B_{hi}=\frac{\mu_0 N_1 I}{4\pi}\left(\frac{-(y-(l_2+l_3/2))}{(y-(l_2+l_3/2))^2+z^2}\right)\times \left(\frac{x+(w_2+w_3/2)}{R_h}-\frac{x+(w_1+w_2+w_3/2)}{R_i}\right) \tag{13}$$

$$B_{ij}=\frac{\mu_0 N_1 I}{4\pi}\left(\frac{(x+(w_1+w_2+w_3/2))}{(x+(w_1+w_2+w_3/2))^2+z^2}\right)\times \left(\frac{y-(l_2+l_3/2)}{R_i}-\frac{y-(l_1+l_2+l_3/2)}{R_j}\right) \tag{14}$$

$$B_{jk}=\frac{\mu_0 N_1 I}{4\pi}\left(\frac{-(y-(l_1+l_2+l_3/2))}{(y-(l_1+l_2+l_3/2))^2+z^2}\right)\times \left(\frac{x+(w_1+w_2+w_3/2)}{R_j}-\frac{x-(w_1+w_2+w_3/2)}{R_k}\right) \tag{15}$$

$$B_{kl}=\frac{\mu_0 N_1 I}{4\pi}\left(\frac{(x-(w_1+w_2+w_3/2))}{(x-(w_1+w_2+w_3/2))^2+z^2}\right)\times \left(\frac{y-(l_1+l_2+l_3/2)}{R_k}-\frac{y-(l_2+l_3/2)}{R_l}\right) \tag{16}$$

$$B_{lm}=\frac{\mu_0 N_1 I}{4\pi}\left(\frac{-(y-(l_2+l_3/2))}{(y-(l_2+l_3/2))^2+z^2}\right)\times \left(\frac{x-(w_1+w_2+w_3/2)}{R_l}-\frac{x-(w_2+w_3/2)}{R_m}\right) \tag{17}$$

$$B_{\mathrm{mn}}=\frac{\mu_0 N_1 I}{4\pi}\left(\frac{(x-(w_2+w_3/2))}{(x-(w_2+w_3/2))^2+z^2}\right)\times\left(\frac{y-(l_2+l_3/2)}{R_{\mathrm{m}}}-\frac{y-(l_3/2)}{R_{\mathrm{n}}}\right) \tag{18}$$

$$B_{\mathrm{no}}=\frac{\mu_0 N_1 I}{4\pi}\left(\frac{-(y-(l_3/2))}{(y-(l_3/2))^2+z^2}\right)\times\left(\frac{x-(w_2+w_3/2)}{R_{\mathrm{n}}}-\frac{x-(w_3/2)}{R_{\mathrm{o}}}\right) \tag{19}$$

$$B_{\mathrm{op}}=\frac{\mu_0 N_1 I}{4\pi}\left(\frac{(x-(w_3/2))}{(x-(w_3/2))^2+z^2}\right)\times\left(\frac{y-(l_3/2)}{R_{\mathrm{o}}}-\frac{y+(l_3/2)}{R_{\mathrm{p}}}\right) \tag{20}$$

$$B_{\mathrm{pq}}=\frac{\mu_0 N_1 I}{4\pi}\left(\frac{-(y+(l_3/2))}{(y+(l_3/2))^2+z^2}\right)\times\left(\frac{x-(w_3/2)}{R_{\mathrm{p}}}-\frac{x-(w_2+w_3/2)}{R_{\mathrm{q}}}\right) \tag{21}$$

$$B_{\mathrm{qr}}=\frac{\mu_0 N_1 I}{4\pi}\left(\frac{(x-(w_2+w_3/2))}{(x-(w_2+w_3/2))^2+z^2}\right)\times\left(\frac{y+(l_3/2)}{R_{\mathrm{q}}}-\frac{y+(l_2+l_3/2)}{R_{\mathrm{r}}}\right) \tag{22}$$

$$B_{\mathrm{rs}}=\frac{\mu_0 N_1 I}{4\pi}\left(\frac{-(y+(l_2+l_3/2))}{(y+(l_2+l_3/2))^2+z^2}\right)\times\left(\frac{x-(w_2+w_3/2)}{R_{\mathrm{r}}}-\frac{x-(w_1+w_2+w_3/2)}{R_{\mathrm{s}}}\right) \tag{23}$$

$$B_{\mathrm{st}}=\frac{\mu_0 N_1 I}{4\pi}\left(\frac{(x-(w_1+w_2+w_3/2))}{(x-(w_1+w_2+w_3/2))^2+z^2}\right)\times\left(\frac{y+(l_2+l_3/2)}{R_{\mathrm{s}}}-\frac{y+(l_1+l_2+l_3/2)}{R_{\mathrm{t}}}\right) \tag{24}$$

$$B_{\mathrm{ta}}=\frac{\mu_0 N_1 I}{4\pi}\left(\frac{-(y+(l_1+l_2+l_3/2))}{(y+(l_1+l_2+l_3/2))^2+z^2}\right)\times\left(\frac{x-(w_1+w_2+w_3/2)}{R_{\mathrm{t}}}-\frac{x+(w_1+w_2+w_3/2)}{R_{\mathrm{a}}}\right) \tag{25}$$

where the expressions for R_{a}, R_{b}, $R_{\mathrm{c}} \cdots R_{\mathrm{s}}$, R_{t} are as folllws:

$$\begin{aligned}
R_a&=\sqrt{(x+(w_1+w_2+w_3/2))^2+(y+(l_1+l_2+l_3/2))^2+z^2}\\
R_b&=\sqrt{(x+(w_1+w_2+w_3/2))^2+(y+(l_2+l_3/2))^2+z^2}\\
R_c&=\sqrt{(x+(w_2+w_3/2))^2+(y+(l_2+l_3/2))^2+z^2}\\
R_d&=\sqrt{(x+(w_2+w_3/2))^2+(y+l_3/2)^2+z^2}\\
R_e&=\sqrt{(x+w_3/2)^2+(y+l_3/2)^2+z^2}\\
R_f&=\sqrt{(x+w_3/2)^2+(y-l_3/2)^2+z^2}\\
R_g&=\sqrt{(x+(w_2+w_3/2))^2+(y-l_3/2)^2+z^2}\\
R_h&=\sqrt{(x+(w_2+w_3/2))^2+(y-(l_2+l_3/2))^2+z^2}\\
R_i&=\sqrt{(x+(w_1+w_2+w_3/2))^2+(y-(l_2+l_3/2))^2+z^2}\\
R_j&=\sqrt{(x+(w_1+w_2+w_3/2))^2+(y-(l_1+l_2+l_3/2))^2+z^2}\\
R_k&=\sqrt{(x-(w_1+w_2+w_3/2))^2+(y-(l_1+l_2+l_3/2))^2+z^2}\\
R_l&=\sqrt{(x-(w_1+w_2+w_3/2))^2+(y-(l_2+l_3/2))^2+z^2}\\
R_m&=\sqrt{(x-(w_2+w_3/2))^2+(y-(l_2+l_3/2))^2+z^2}\\
R_n&=\sqrt{(x-(w_2+w_3/2))^2+(y-l_3/2)^2+z^2}\\
R_o&=\sqrt{(x-w_3/2)^2+(y-l_3/2)^2+z^2}\\
R_p&=\sqrt{(x-w_3/2)^2+(y+l_3/2)^2+z^2}\\
R_q&=\sqrt{(x-(w_2+w_3/2))^2+(y+l_3/2)^2+z^2}\\
R_r&=\sqrt{(x-(w_2+w_3/2))^2+(y+(l_2+l_3/2))^2+z^2}\\
R_s&=\sqrt{(x-(w_1+w_2+w_3/2))^2+(y+(l_2+l_3/2))^2+z^2}\\
R_t&=\sqrt{(x-(w_1+w_2+w_3/2))^2+(y+(l_1+l_2+l_3/2))^2+z^2}
\end{aligned} \tag{26}$$

In summary, the total flux density B_{total} in the Z-axis direction of the flux density generated by the transmitting coil at any point P is shown in (27).

$$\begin{aligned}
B_{\mathrm{total}} = {} & B_{\mathrm{ab}}+B_{\mathrm{bc}}+B_{\mathrm{cd}}+B_{\mathrm{de}}+B_{\mathrm{ef}}+\\
& B_{\mathrm{fg}}+B_{\mathrm{gh}}+B_{\mathrm{hi}}+B_{\mathrm{ij}}+B_{\mathrm{jk}}+\\
& B_{\mathrm{kl}}+B_{\mathrm{lm}}+B_{\mathrm{mn}}+B_{\mathrm{no}}+B_{\mathrm{op}}+\\
& B_{\mathrm{pq}}+B_{\mathrm{qr}}+B_{\mathrm{rs}}+B_{\mathrm{st}}+B_{\mathrm{ta}}
\end{aligned} \tag{27}$$

According to the flux density method, the mutual inductance between a single-turn stepped transmitting coil and a single-turn rectangular receiving coil is calculated as follows:

$$M=\frac{\oint_D B\cdot \mathrm{d}s}{I} \tag{28}$$

where s denotes the area where the receiving coil is located, I denotes the current on the transmitting coil.

TABLE I
Optimised Range of EESC Structural Parameters

Parameters	Optimisation Scope
L_1	50 ~ 150 mm
L_2	50 ~ 150 mm
L_3	300 ~ 400 mm
W_1	100 ~ 200 mm
W_2	100 ~ 200 mm
W_3	100 ~ 200 mm
L_{rxs}	50 ~ 100 mm
W_{rxs}	500 ~ 600 mm
L_{rx}	400 ~ 500 mm
W_{rx}	500 ~ 700 mm
N_{tx1}	5 ~ 15
N_{txs}	15 ~ 25
N_{rx}	15 ~ 25

In order to facilitate the numerical calculation, the rectangular receiving coil is subdivided, it is assumed that the magnetic flux density at each place in each small rectangle after subdividing is uniformly distributed, which is equal to the magnetic flux density at the centre of the small rectangle. The length l_4 of the receiving coil is subdivided into N_L parts, the width w_4 of the receiving coil is subdivided into N_W parts, and the length and width of the subdivided small rectangle are d_L and d_W, respectively. The mutual inductance between single turn coils is calculated as follows

$$M_{11}=\frac{d_L d_W}{I}\sum_{i=1}^{N_L}\sum_{j=1}^{N_W}B_{ij} \tag{29}$$

When the stepped coil calculates the mutual inductance of the n-th turn to the rectangular receiving coil, in order to ensure that the shape of the stepped coil remains unchanged, the inner diameters of the transmitting coils l_2, w_1, and w_2 remain unchanged, and l_1, l_3, and w_3 satisfy the following rule of law:

$$l_{1\_N}=l_1+2(N-1)R_{line} \tag{30}$$

$$l_{3\_N}=l_3-2(N-1)R_{line} \tag{31}$$

$$w_{3\_N}=w_3+2(N-1)R_{line} \tag{32}$$

where l_{1_N}, l_{3_N}, and w_{3_N} are the lengths of the N-th turn l_1, l_3, and w_3, respectively, and R_{line} is the wire diameter.

According to the superposition theorem, the following for-mula for calculating the mutual inductance between multi-turn rectangular coils can be obtained:

$$M=\sum_{m=1}^{N_T}\sum_{n=1}^{N_R}M_{mn} \tag{33}$$

where N_T denotes the number of turns of the transmitting coil, N_R denotes the number of turns of the receiving coil, and M_{mn} denotes the mutual inductance between the m-th turn of $Coil_1$ and the n-th turn of $Coil_2$.

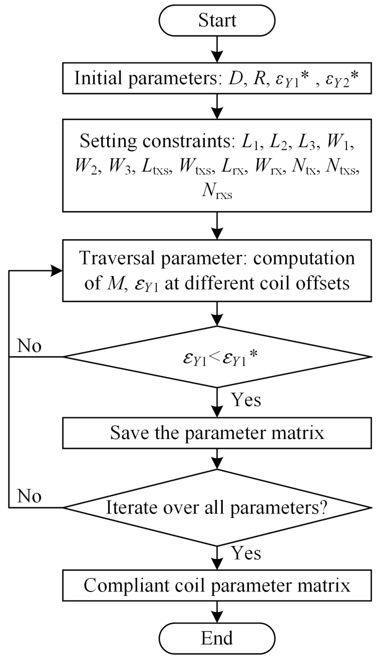

Fig. 5. Flowchart for the coil parameter optimization.

IV. EESC Coil Optimisation

The mutual inductance M is taken as the optimisation objective, the parameters of the EESC structure are optimised based on the principle of minimum mutual inductance fluctuation in order to achieve a strong anti-offset performance. To ensure the mutual inductance and anti-offset performance of the coil structure, the coil structure parameters and core parameters are optimised respectively. Firstly, the coil parameters are optimised to find the coil structure parameter matrix that meets the requirements. Secondly, the core structure is analysed on the basis of the coil parameters and the optimisation of the core size parameters is completed.

A. Optimisation of Coil Parameters

1) Objective function

The key parameters influencing the mutual inductance M of the coil are analyzed and optimized, specifically focusing on the dimensional parameters of the coil structure.

$$M=f(L_1,L_2,L_3,W_1,W_2,W_3,L_{txs},W_{txs},L_{rx},W_{rx},N_{tx},N_{txs},N_{rx}) \tag{34}$$

2) Setting constraints

The mutual inductance M of the coil is dependent on both the inner diameter and the number of turns. The constraints on the coil structure are determined based on the practical application. The range of coil parameters to be optimized is presented in Table I.

3) Coil parameter optimisation process

TABLE II
EESC Structure Dimension Parameter

Parameters	Value
L_1	100 mm
L_2	50 mm
L_3	360 mm
W_1	150 mm
W_2	150 mm
W_3	100 mm
L_{rxs}	50 mm
W_{rxs}	600 mm
L_{rx}	430 mm
W_{rx}	650 mm
N_{tx1}	8
N_{txs}	20
N_{rx}	20

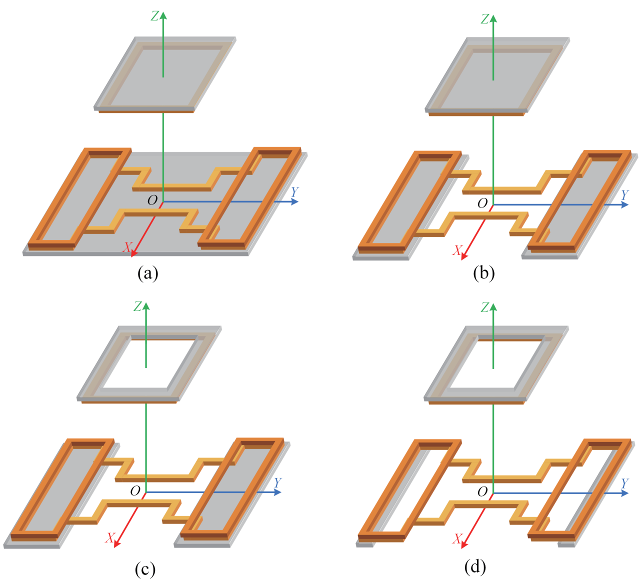

Fig. 6. Schematic diagrams of different magnetic core structures. (a) Conventional non-skeletonised core structure. (b) Separate core structure. (c) Separate skeletonised core structure. (d) Optimised core structure.

The parameter optimization of the EESC structure is conducted based on the principle of minimizing mutual inductance fluctuations. This optimization ensures that the mutual inductance and its fluctuation rate meet the specified requirements when the coil is offset at various positions. The mutual inductance fluctuation rate is defined as the rate of change in mutual inductance when the coil is displaced along the Y-axis. The formula for this fluctuation rate is as follows:

$$\varepsilon_{Y1}=\left|\frac{M_{\Delta Y}-M_0}{M_0}\right|\times 100\% \tag{35}$$

where M_0 denotes the mutual inductance between the coils when they are aligned, $M_{\Delta Y}$ denotes the mutual inductance between the coils when the coil are offset in the Y-axis.

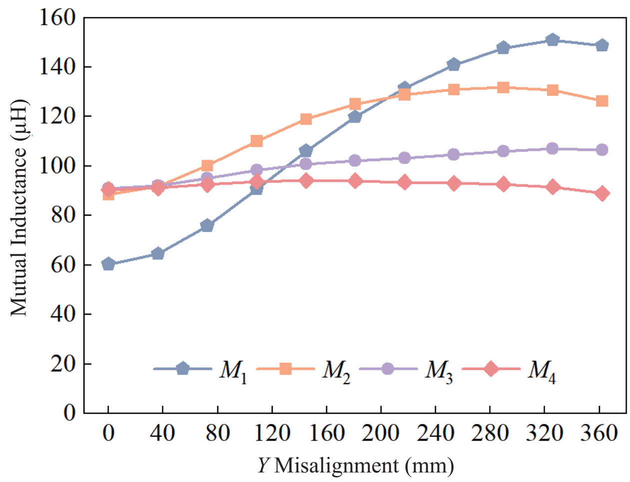

Fig. 7. Trend of mutual inductance of different magnetic core structures.

The optimization flow chart of coil parameters based on the principle of minimum mutual inductance fluctuation is shown in Fig. 5.

The specific steps of the optimization process are as follows: First, the transmission distance D between the coils is set to 150 mm, the wire diameter is 4 mm, the mutual inductance fluctuation rates ε_{Y1}^* are set to 5%. Second, relevant constraints are established according to the range of coil parameters provided in Table I. Next, the optimized parameters are traversed to calculate the mutual inductance M at various positional offsets. The mutual inductance fluctuation rate ε_{Y1} is calculated according to (35). ε_{Y1} is judged whether satisfies $\varepsilon_{Y1}<\varepsilon_{Y1}^*$, when it satisfies the above conditions, the corresponding parameter matrix is saved. If the result is not satisfied, the program traverses the next set of parameters.

Finally, after all parameters have been traversed, the output meets the required coil parameter matrix for the subsequent core optimization process. By optimising the parameters of the EESC structure, the dimensional parameters of the transmitter-side coil and receiver-side coil are shown in Table II.

B. Optimisation of Core Parameters

In order to improve the offset resistance of the coil structure and the mutual inductance between the coils, magnetic materials are usually added to the coupling coils. The common magnetic materials are ferrites. In this section, in order to design a core structure that fits the changing characteristics of the mutual inductance of the coils, the influence of different shapes of the core structure on the mutual inductance of the coils is analysed on the basis of the EESC structure, the parameters of the core structure are optimised after the shape is determined. The evolution of the core structure is shown in Fig. 6. Fig. 6(a) shows the traditional non-skeletonised core structure with mutual inductance denoted as M_1; Fig. 6(b) shows the separated core structure with mutual inductance denoted as M_2; Fig. 6(c) shows the separated skeletonised core structure with mutual inductance denoted as M_3; and Fig. 6(d) shows the optimised core

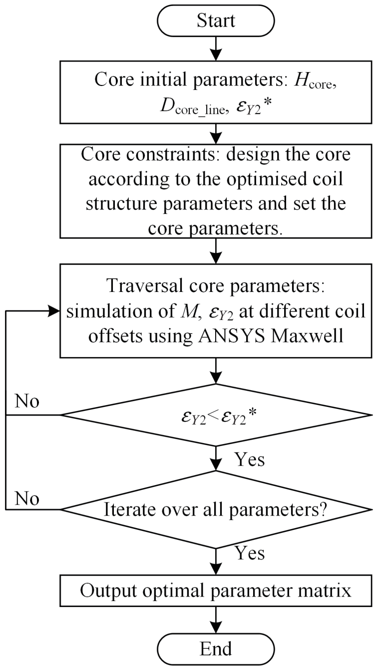

Fig. 8. Flowchart for the magnetic core parameter optimization.

structure of this paper with mutual inductance denoted as M_4.

Fig. 7 shows the trend of mutual inductance of coils with different core structures. When the conventional non-skeletonised core structure is used, the mutual inductance M_1 between the coils increases from 60.27 μH to 148.51 μH as the coil position is shifted, the mutual inductance between the coils decreases instead of increasing when it is positively aligned, and the mutual inductance fluctuation rate is as high as 150%. In order to make the core structure fit the structural characteristics of the coils better, the core on the transmitter side adopts a separated structure using two smaller bar-shaped cores, which are placed in the overlapping part of the main coil and the compensation coil. With the separated core structure, the mutual inductance M_2 between the coils increases from 88.37 μH to 126.21 μH with the coil offset, and the mutual inductance fluctuation rate decreases to 49%. The use of the separated core structure solves the problem of reducing the mutual inductance of the coils when the conventional non-skeletonised core structure is positively aligned, and saves 38.8% of the core material compared to the conventional non-skeletonised core structure. Subsequently, based on the use of the separated core structure on the transmitter side, the core on the receiver side adopts a centre skeleton design, which is designed to provide better magnetic path access to the coil. With the offset of the coils, the mutual inductance M_3 between the coils increases from 90.95 μH to 106.37 μH with a maximum mutual inductance fluctuation of only 16.9%. It can be seen that for the edge-enhanced stepped coil structure proposed in this chapter, the most fitting core structure is a separated core on the transmitter side and a skeletonised core on the receiver side. After determining the approximate shape of the core structure, a core parameter optimisation strategy based on the principle of minimising mutual inductance fluctuation is proposed to optimise the dimensions

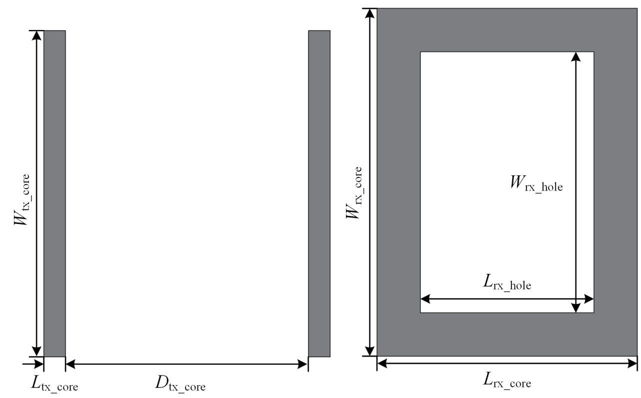

Fig. 9. Magnetic core structure diagram.

of the separated core on the transmitter side and the separation spacing, as well as the dimensions of the skeletonised core on the receiver side and the size of the skeleton, in order to address the problem of mutual inductance fluctuation caused by coil offset.

The flowchart of core parameter optimisation based on the principle of minimum mutual inductance fluctuation is shown in Fig. 8.

1) Core parameter setting

The core of the transmitting coil is located below the transmitting coil, and the core of the receiving coil is located above the receiving coil. The given core thickness H_{core} is 10 mm, the core and the winding line are close to each other, the spacing between the core and the winding line D_{core_line} is nearly 0, and the mutual inductance fluctuation rate ε^*_{Y2} is set to 5%.

2) Setting core constraints

The core structure is designed based on the optimized coil structure dimensions. The coil design is constrained by the actual core structure, which imposes several limitations. These constraints include the transmitting side core dimensions,the receiving side core dimensions and core skeleton dimensions. These constraints ensure that the core structure is appropriately sized and positioned to support the optimized coil configuration and achieve the desired performance.

3) Core parameter optimization

The mutual inductance between the transmitting and receiving coils can be measured by ANSYS Maxwell simulation software, the mutual inductance fluctuation rate ε_{Y2} is calculated according to (36). ε_{Y2} is judged whether satisfies $\varepsilon_{Y2} < \varepsilon^*_{Y2}$, when it satisfies the above conditions, the corresponding parameter matrix is saved. When the result does not satisfy the requirements, the program traverses the next set of parameters. Finally, when all the parameters have

$$\varepsilon_{Y1}=\left|\frac{M^*_{\Delta Y}-M^*_0}{M^*_0}\right|\times 100\% \qquad (36)$$

where M^*_0 denotes the mutual inductance between the coils when they are aligned, $M^*_{\Delta Y}$ denotes the mutual inductance between the coils when they are offset in the Y-axis.

According to the above optimisation, the transmitting-side

TABLE III
EESC Structure Magnetic Core Dimension Parameter

Parameters	Value
L_{tx_core}	50 mm
W_{tx_core}	750 mm
D_{tx_core}	560 mm
L_{rx_core}	600 mm
W_{rx_core}	800 mm
L_{rx_hole}	400 mm
R_{rx_hole}	600 mm
H_{core}	10 mm

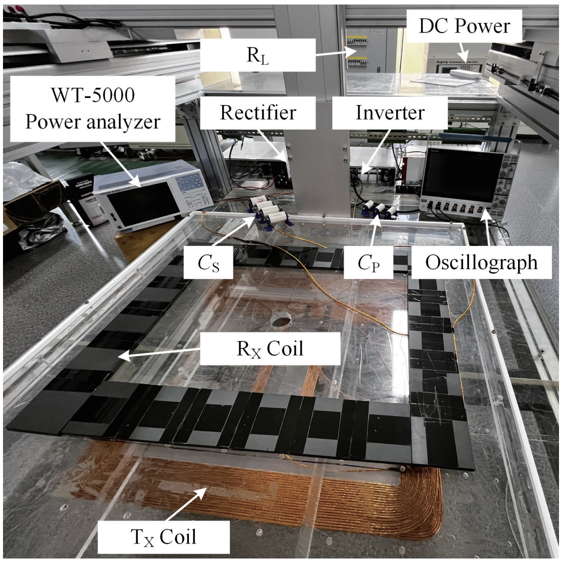

Fig. 10. Prototype of the WPT system.

core adopts a separated structure, which is symmetrically placed on the left and right sides, and the receiving-side core is a hollow structure in the middle, as shown in Fig. 6(d), and the variation curve of the coil mutual inductance is shown in Fig. 7 as M_4, and the mutual inductance fluctuation rate is less than 5%. The core plan view is shown in Fig. 9, and the core size parameters are shown in Table III.

V. Experimental Verification

A. Prototype

To verify the feasibility and effectiveness of the proposed WPT system, a 500 W experimental prototype of the wireless energy transmission system is constructed. This prototype is used to assess the anti-offset performance of the system, ensuring its reliability under various operating conditions.

Based on the coil size parameters provided in Table II, physical coils were wound, and the experimental prototype was constructed on a 3D motion platform. Fig. 10 displays the experimental prototype of the system, which includes the components of the WPT system, such as the DC power supply, inverter module, rectifier module, transmitter coil T_x, transmitter-side compensation capacitor C_P, receiver coil R_x, receiver-side compensation capacitor C_S, and load resistor. Fig. 11 shows the EESC structure. The inverter and rectifier components utilize silicon carbide power devices, specifically the model C3M0075120D. The experimental platform consists of a three-dimensional moving structure, featuring a stationary lower level and a three-dimensionally movable upper level. The transmitting coil is positioned on the lower level, while the receiving coil is located on the upper movable platform. Offset control is achieved through the 3D platform interface controller. The main parameters of the prototype WPT system are summarized in Table IV.

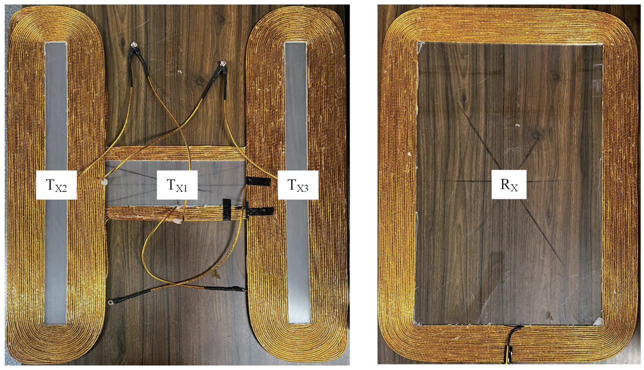

Fig. 11. EESC structure.

TABLE IV
Main Parameters of the WPT System Prototype

Parameters	Value	Parameter	Value
U_{DC} (V)	170.0	f (kHz)	85
L_P (μH)	898	L_P^* (μH)	1038
C_P (nH)	3.67	C_P^* (nF)	3.16
L_S (μH)	521	L_S^* (μH)	804
C_S (nF)	6.54	C_S^* (nF)	4.18
M (μH)	64.05	M^* (μH)	89.1

B. Mutual Inductance Analysis

Firstly, MATLAB is used to develop a program for calculating the mutual inductance of the coreless coil, allowing for the determination of the theoretical mutual inductance value M_c for the EESC structure. Secondly, finite element software is employed for modeling and simulation to obtain the simulated coupling coefficient M_s of the EESC structure. Finally, the self-inductance and mutual inductance of the physical coil are measured using an impedance analyzer to obtain the experimental value M_e. The error between the theoretical value and the experimental value is defined as ε_c, and the error between the simulation value and the experimental value is defined as ε_s. These errors are calculated using the following formulas:

TABLE V
MUTUAL INDUCTANCE AND ERROR WITHOUT MAGNETIC CORE AT OFFSET ALONG Y-AXIS

ΔY/mm	M_C	M_S	M_e	ε_C	ε_S
0	64.22	65.81	64.05	0.27%	2.75%
36.2	64.54	66.03	64.05	0.77%	3.09%
72.4	65.31	66.58	64.69	0.96%	2.92%
108.6	66.13	67.23	65.33	1.22%	2.91%
144.8	66.68	67.64	65.79	1.35%	2.81%
181.0	66.89	67.73	65.66	1.87%	3.15%
217.2	66.85	67.58	65.56	1.97%	3.08%
253.4	66.62	67.27	65.04	2.43%	3.43%
289.6	66.13	66.71	64.43	2.64%	3.54%
325.8	65.04	65.53	63.05	3.16%	3.93%
362.0	62.72	63.05	60.95	2.90%	3.45%

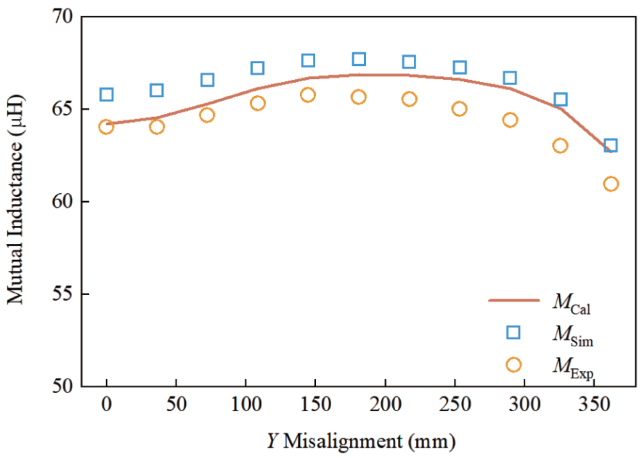

Fig. 12. Variation curves of coil mutual inductance without magnetic core at offset along the Y-axis direction.

$$\varepsilon_c = \left| \frac{M_c - M_e}{M_e} \right| \times 100\% \tag{37}$$

$$\varepsilon_s = \left| \frac{M_s - M_e}{M_e} \right| \times 100\% \tag{38}$$

Table V presents the mutual inductance values and associated errors for the coreless coil when offset along the Y-axis. From the table, it can be observed that the experimental mutual inductance of the coil is 64.05 μH when it is aligned. When the coil is offset by 50% (362 mm) of the outer diameter length of the launching coil along the Y-axis, the experimental mutual inductance decreases to 60.95 μH. The fluctuation rate of the mutual inductance at this offset is 4.84%. The trend of the mutual inductance of the EESC structure with respect to the offset distance along the Y-axis shows an initial increase followed by a decrease, which aligns with the theoretical analysis of the magnetic field behavior in the EESC structure. The error ε_c is less than 3.16%, and the error ε_s is less than 3.93%. To provide a more intuitive understanding of the coil's behavior, Fig. 12 shows the change curve of the mutual inductance of the coreless coil when offset along the Y-axis. From this curve, it can be seen that the mutual inductance of the coil remains relatively stable around 64 μH.

TABLE VI
MUTUAL INDUCTANCE AND ERROR WITH MAGNETIC CORE AT OFFSET ALONG Y-AXIS

ΔY/mm	M_S	M_e	ε_S
0	90.49	89.10	1.56%
36.2	91.14	88.74	2.70%
72.4	92.57	89.72	3.18%
108.6	93.76	90.74	3.33%
144.8	94.18	91.34	3.11%
181.0	93.95	91.34	2.86%
217.2	93.50	91.22	2.50%
253.4	93.12	90.71	2.66%
289.6	92.61	90.36	2.49%
325.8	91.63	89.11	2.83%
362.0	89.01	86.19	3.27%

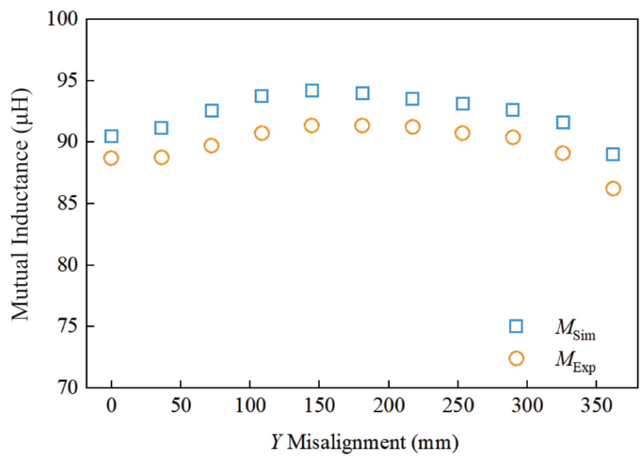

Fig. 13. Variation curves of coil mutual inductance with magnetic core at offset along the Y-axis direction.

Table VI presents the mutual inductance values and associated errors for the coil with a magnetic medium when offset along the Y-axis. The experimental mutual inductance is 89.10 μH when the coils are aligned. When the coil is offset by 50% (362 mm) of the outer diameter length of the launching coil along the Y-axis, the experimental mutual inductance decreases to 86.19 μH, with a fluctuation rate of 3.27%. The error ε_s is less than 3.33%. To provide a more intuitive view of the coil's behavior, Fig. 13 shows the change curve of the mutual inductance for the coil with magnetic core when offset along the Y-axis. The mutual inductance of the coil changes smoothly and remains relatively stable at about 89.1 μH.

In summary, both the EESC structures without magnetic core and those with magnetic cores demonstrate strong offset

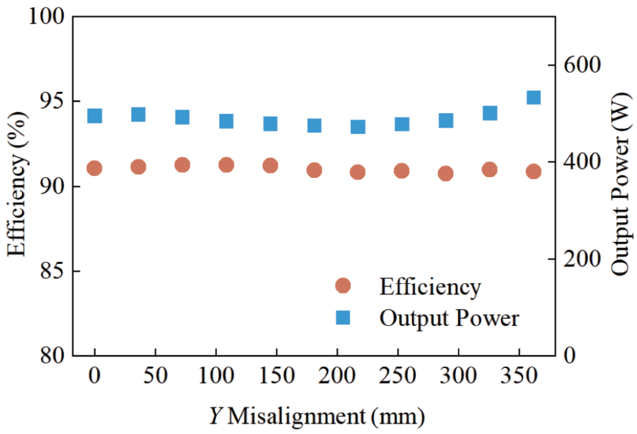

Fig. 14. Variation curves of coil mutual inductance with magnetic core at offset along the *Y*-axis direction.

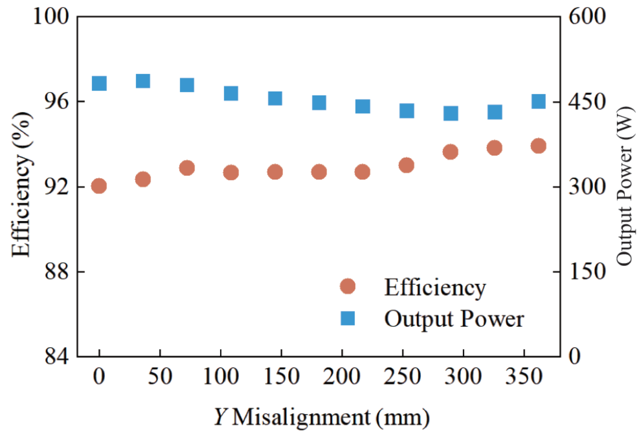

Fig. 16. Variation curves of system output power and transmission efficiency with magnetic core at offset along the *Y*-axis direction.

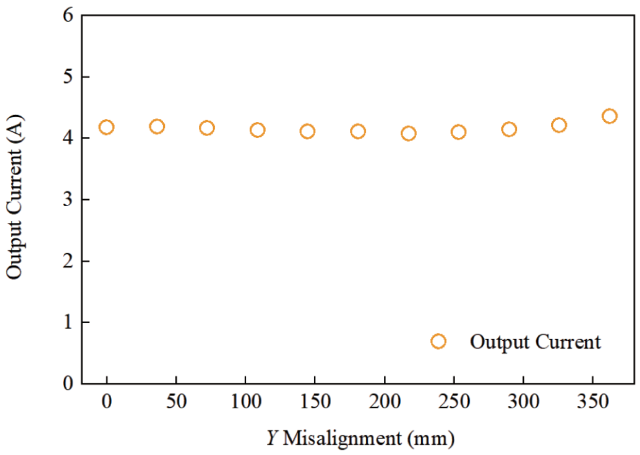

Fig. 15. Variation curves of system output current and without magnetic core at offset along the *Y*-axis direction.

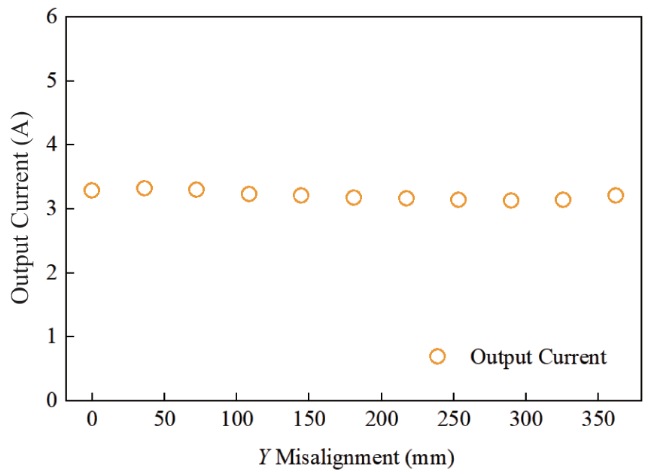

Fig. 17. Variation curves of system output current and with magnetic core at offset along the *Y*-axis direction.

resistance, capable of withstanding 50% (362 mm) offset of the outer diameter of the transmitter coil in the *Y*-axis direction. In all cases, the mutual inductance fluctuation rate remains below 5%, indicating robust performance even under significant displacement.

C. System Performance Analysis

Fig. 14 shows the variation curves of output power and transmission efficiency of the WPT system without magnetic medium with offset distance. From Fig. 11, it can be seen that the output power of the system is 495.44 W when the coil is aligned. When the offset distance is within 362 mm, the maximum output power and minimum output power are 533.9 W and 473.39 W. The transmission efficiency of the system has a tendency to increase and then decrease when offset along the *Y*-axis. This behavior aligns with the mutual inductance fluctuations shown in Fig. 9, where the transmission efficiency peaks at 91.3%. The maximum fluctuations in transmission efficiency and output power are 0.21% and 7.76%, respectively.

Fig. 15 shows the output current variation curve of the coreless system, from which it can be seen that the system output current is 4.18 A when the coil is aligned, and when the coil offset distance is within 50% (362 mm) of the outer diameter length of the transmitter coil, the maximum and minimum output currents of the system are 4.36 A and 4.08 A, respectively, and the output current fluctuation rate is less than 5%.

Fig. 16 shows the relationship between the output power and transmission efficiency of the WPT system with magnetic media and the offset distance. It can be seen that the transmission efficiency and output power are 92.04% and 482.79 W when the coil is aligned. When the offset distance is within 362 mm, the maximum transmission efficiency and minimum measured efficiency are 93.92% and 92.04%, respectively, and the maximum output power and minimum output power are classified as 486.71 W and 429.78 W, the system efficiency and power fluctuations are 0.2% and 10.98%, respectively. When offset along the *Y*-axis direction, the transmission efficiency shows a gradual increasing trend, and the transmission efficiency of the system is as high as 93.92%.

Fig. 17 shows the output current variation curve of the sys-

TABLE VII
MPPT Algorithm Performance for Different PV Array Topologies under Shade Case-III

Ref.	Coil Structure	Transmission Distance / mm	Maximum Offset Distance / mm	Offset Rate / %	Fluctuation Rate / %	Output Power / W
[18]	FSC	170	200	50%	20.2%	500
[19]	Flat Solenoid	170	120	40%	12.3%	500
[24]	DQDD	130	150	38.4%	55%	500
[26]	ISC	150	225	50%	3.81%	108.8
Proposed	EESC	150	362	50%	3.27%	495.6

Note: Offset ratio equals the *X*/*Y* direction coil offset distance / the maximum *X*/*Y* direction coil outer length.

tem with magnetic core. It can be seen that the system output current is 3.29 A when the coil is aligned, and when the coil offset distance is within 50% (362 mm) of the outer diameter length of the transmitter coil, the maximum and minimum output currents of the system are 3.32 A and 3.13 A, respectively, and the fluctuation rate of the output current is less than 5%.

D. Comparison of Anti-Offset Performance

In order to demonstrate the resistance to deflection of the proposed coil structure and the innovativeness of the optimised design method, the WPT system proposed in this paper is compared with the existing literature, as shown in Table VII.

Compared to the solenoidal coupling structure mentioned in [18]−[19], the coil structure proposed in this paper has a larger offset distance and offset rate with a smaller offset resistance. Compared to the literature [24]−[25], the coil structure proposed in this paper has a larger offset distance while the mutual inductance fluctuation rate is only 3.27%, which provides a better anti-offset performance.

VI. Conclusion

In this paper, an edge-enhanced stepped coil (EESC) structure is proposed to improve the anti-offset performance of the system. Firstly, the model of the edge-enhanced stepped coil structure is analyzed, and the mutual inductance characteristics of this structure are examined. Secondly, a new method for calculating the mutual inductance of stepped coils is introduced, based on the Biot-Savart law. Subsequently, an optimization strategy is developed, focusing on minimizing the fluctuation of mutual inductance, to optimize both the coil size and the core size parameters. Finally, to validate the proposed methods, a 500 W experimental prototype is constructed. Simulation and experimental results confirm the accuracy of the coil mutual inductance calculation method and demonstrate the robust offset resistance of the coil structure. The experimental findings show that the mutual inductance fluctuation rate of the EESC, both with and without a magnetic core, remains below 5% when the system is offset along the *Y*-axis by 50% (362 mm) of the outer diameter of the transmitting coil. Additionally, the error between the measured mutual inductance and the theoretical and simulated values does not exceed 5%. The transmission efficiency of the coreless EESC system is 91.3%, with an output current of 4.18 A and a fluctuation rate of the output current less than 5%. The EESC system with magnetic core achieves a transmission efficiency of 93.92%, an output current of 3.29 A, a fluctuation rate of the output current of less than 5%. Therefore, the EESC structure proposed in this study is well-suited for dynamic wireless charging of electric vehicles. Further research will focus on improving the anti-offset performance of the EESC coil in the *X*-axis direction.

References

[1] Y. Zhang, W. Pan, C. Liu, Z. Shen, Y. Wu, Y. Zhuang, and Z. Li, "Interoperability study of electric vehicle wireless charging system based on three decoupled nonoverlapping unipolar transmitting coils," in *IEEE Transactions on Transportation Electrification*, vol. 10, no. 4, pp. 8630–8639, Dec. 2024.

[2] H. Zhou, Z. Shen, Y. Wu, X. Chen, and Y. Zhang, "A stable dynamic electric vehicle wireless charging system based on triple decoupling receiving coils and a novel triple-diode rectifier," in *IEEE Transactions on Industrial Electronics*, vol. 71, no. 10, pp. 12011–12018, Oct. 2024.

[3] Z. Shen, H. Zhou, R. Xie, Y. Zhuang, X. Mao, and Y. Zhang, "A strong offset-resistant electric vehicle wireless charging system based on dual decoupled receiving coils," in *IEEE Transactions on Industrial Electronics*, vol. 71, no. 11, pp. 15216–15219, Nov. 2024.

[4] X. Wu, P. Sun, S. Yang, L. He, and J. Cai, "Review on underwater wireless power transfer technology and its Application," in *Transactions of China Electrotechnical Society*, vol. 34, no. 8, pp. 1559–1568, Apr. 2019.

[5] H. Guo, X. Zhang, Q. Yang, L. Sha, F. Wang, and Z. Zhu, "Review of research and application of spatial omnidirectional wireless power transmission technology," in *Proceedings of the CSEE*, vol. 42, no. 24, pp. 9006–9022, Dec. 2022.

[6] D. Wang, J. Zhang, C. Zhu, Z. Bie, and S. Cui, "Review of progress in the study of marine environment effects on underwater wireless power transfer systems," in *Transactions of China Electrotechnical Society*, vol. 40, no. 3, pp. 653–675, Feb. 2025.

[7] Y. Yang, W. Jia, D. Liang, J. Xue, and Y. Li, "A self-switching wireless power transfer system based on hybrid topology of LCC-LCC/S with constant current and constant voltage," in *Transactions of China Electrotechnical Society*, vol. 38, no. 18, pp. 4823–4837+4852, Sept. 2023.

[8] V. -B. Vu, D. -H. Tran, and W. Choi, "Implementation of the constant current and constant voltage charge of inductive power transfer systems with the double-sided LCC compensation topology for electric vehicle battery charge applications," in *IEEE Transactions on Power Electronics*, vol. 33, no. 9, pp. 7398–7410, Sept. 2018.

[9] L. Ji, M. Zhang, B. Qian, and H. Sun, "A series of hybrid WPT systems with automatic switching between constant-current and constant-voltage modes on the secondary side," in *IEEE Journal of Emerging and Selected Topics in Power Electronics*, vol. 11, no. 1, pp. 361–371, Feb. 2023.

[10] K. Chen, Y. Jiang, T. Tan, Q. Lin, J. Li, and Z. Zhao, "Research on 350kW high power wireless power transfer system for rail transit," in

Transactions of China Electrotechnical Society, vol. 37, no. 10, pp. 2411–2421+2445, May 2022.

[11] L. Wu, G. Li, Z. Zhang, and H. Ma, "A wireless power transfer system topology with automatic switching characteristics of constant current and constant voltage output for electric vehicle charging" in *Transactions of China Electrotechnical Society*, vol. 35, no. 18, pp. 3781–3790, Sept. 2020.

[12] J. Li, C. Zhu, J. Xie, F. Lu, and X. Zhang, "Design and implementation of high-misalignment tolerance WPT system for underwater vehicles based on a variable inductor," in *IEEE Transactions on Power Electronics*, vol. 38, no. 10, pp. 11726–11737, Oct. 2023.

[13] Y. Chen, B. Yang, X. Zhou, Q. Li, Z. He, R. Mai, and J.-S. Lai, "A hybrid inductive power transfer system with misalignment tolerance using quadruple-D quadrature pads," in *IEEE Transactions on Power Electronics*, vol. 35, no. 6, pp. 6039–6049, Jun. 2020.

[14] Y. Zhang, C. Liu, M. Zhou, and X. Mao, "A novel asymmetrical quadrupolar coil for interoperability of Unipolar, Bipolar, and Quadrupolar coils in electric vehicle wireless charging systems," in *IEEE Transactions on Industrial Electronics*, vol. 71, no. 4, pp. 4300–4303, Apr. 2024.

[15] J. Ren, K. Zhou, H. Li, Y. Liu, and R. Mai, "Study of dual coupled LCL topology IPT system based on DDQ coils and its anti-misalignment method," in *Proceedings of the CSEE*, vol. 39, no. 09, pp. 2778–2788, May 2019.

[16] Z. Li, J. Li, S. Li, Y. Yu, and J. Yi, "Design and optimization of asymmetric and reverse series Coil structure for obtaining quasi-constant mutual inductance in dynamic wireless charging system for electric vehicles," in *IEEE Transactions on Vehicular Technology*, vol. 71, no. 3, pp. 2560–2572, Mar. 2022.

[17] Y. Chen, B. Yang, Z. Kou, Z. He, G. Cao, and R. Mai, "Hybrid and reconfigurable IPT systems with high-misalignment tolerance for constant-current and constant-voltage battery charging," in *IEEE Transactions on Power Electronics*, vol. 33, no. 10, pp. 8259–8269, Oct. 2018.

[18] Y. Yao, S. Gao, Y. Wang, X. Liu, X. Zhang, and D. Xu, "Design and optimization of an electric vehicle wireless charging system using interleaved Boost converter and flat solenoid coupler," in *IEEE Transactions on Power Electronics*, vol. 36, no. 4, pp. 3894–3908, Apr. 2021.

[19] Y. Wang, K. Lu, Y. Yao, X. Liu, and D. Xu, "An electric vehicle (EV)-oriented wireless power transfer system featuring high misalignment tolerance," in *Proceedings of the CSEE*, vol. 39, no. 13, pp. 3907–3917, Jul. 2019.

[20] Y. Peng, B. Zhang, B. Yang, S. He, Y. Chen, and R. Mai, "A high misalignment tolerant inductive power transfer system based on double solenoid quadrature pad," in *Proceedings of the CSEE*, vol. 42, no. 20, pp. 7352–7363, Oct. 2022.

[21] M. Budhia, J. T. Boys, G. A. Covic, and C. -Y. Huang, "Development of a single-sided flux magnetic coupler for electric vehicle IPT charging systems," in *IEEE Transactions on Industrial Electronics*, vol. 60, no. 1, pp. 318–328, Jan. 2013.

[22] A. Zaheer, G. A. Covic, and D. Kacprzak, "A Bipolar Pad in a 10-kHz 300-W distributed IPT system for AGV applications," in *IEEE Transactions on Industrial Electronics*, vol. 61, no. 7, pp. 3288–3301, Jul. 2014.

[23] S. Kim, G. A. Covic, and J. T. Boys, "Tripolar Pad for inductive power transfer systems for EV charging," in *IEEE Transactions on Power Electronics*, vol. 32, no. 7, pp. 5045–5057, Jul. 2017.

[24] H. Xiao, Q. Zhou, S. Xiong, Y. Yang, and S. Xie, "Wireless power transfer system based on double-layer quadrature double-D coupling structure with anti-misalignment and anti-deflection," in *Transactions of China Electrotechnical Society*, vol. 37, no. 16, pp. 4004–4018, Aug. 2022.

[25] Z. Li, S. Li, J. Li, R. Zou, and S. Huang, "Mutual inductance calculation and optimization of multi-receiver positive and negative series coil structure in dynamic wireless power transfer systems," in *Transactions of China Electrotechnical Society*, vol. 36, no. 24, pp. 5153–5164, Dec. 2021.

Chenxi Zhang received the bachelor's degree in electrical engineering and automation from Hunan Institute of Technology, Hengyang, China, in 2021 and the master's degree in electronic information from Hunan University of Technology, Zhuzhou, China in the year 2025. His research interests include wireless power transfer systems.

Zhongqi Li received the master's degree from Hunan University of Technology, Zhuzhou, China in 2012, and the Ph.D. degree from the Hunan University in the year 2016. From 2016, he is working associate professor in Hunan University of Technology, China. From 2020, he is now working postdoctoral fellow in Hunan University. His research interests include wireless power transfer systems and softswitching power converters.

Changxuan Hu received a bachelor's degree in Electrical Engineering form Henan Polytechnic University, Jiaozuo, China, in 2021 and the master's degree in control science and engineering from Hunan University of Technology, Zhuzhou, China in 2025. His research interests include wireless power transfer.

Jianbin Wang received the bachelor's degree in electronic information from Shandong Huayu University of Technology, Dezhou, China, in 2022 and the master's degree in electronic information from Hunan University of Technology, Zhuzhou, China in 2025. His research interests include wireless power transfer systems.